minerals

MDPI

Article

Use of Natural Clinoptilolite in the Preparation of an Efficient Adsorbent for Ciprofloxacin Removal from Aqueous Media

Barbara Kalebić [1], Jelena Pavlović [2], Jelena Dikić [2], Aleksander Rečnik [3], Sašo Gyergyek [3], Nikola Škoro [4] and Nevenka Rajić [1,*]

[1] Faculty of Technology and Metallurgy, University of Belgrade, 11120 Belgrade, Serbia; bkalebic@tmf.bg.ac.rs
[2] Innovation Centre of Faculty of Technology and Metallurgy, University of Belgrade, 11120 Belgrade, Serbia; jelena.pavlovic@tmf.bg.ac.rs (J.P.); jdikic@tmf.bg.ac.rs (J.D.)
[3] Jožef Stefan Institute, 1000 Ljubljana, Slovenia; aleksander.recnik@ijs.si (A.R.); saso.gyergyek@ijs.si (S.G.)
[4] Institute of Physics, University of Belgrade, 11080 Belgrade, Serbia; nskoro@ipb.ac.rs
* Correspondence: nena@tmf.bg.ac.rs

Abstract: The adsorption of the antibiotic ciprofloxacin (CIP) from an aqueous solution by natural zeolite, the calcium-rich clinoptilolite (CLI), and magnetite-coated CLI (MAG-CLI) was investigated. Both CLI and MAG-CLI showed a high adsorption affinity towards CIP at 283, 288 and 293 K at a pH of 5. Adsorption kinetics studied for the initial concentrations of 15–75 mg CIP dm^{-3} follow Lagergren's pseudo-second order equation and the adsorption is best represented by the Langmuir model. The adsorption mechanism involves strong electrostatic interactions between negatively charged aluminosilicate lattice and the cationic form of CIP accompanied by an ion-exchange reaction. Magnetite coverage (approx. 12 wt.%) induces magnetism, which can facilitate the separation process. The coverage does not influence the adsorption activity of CLI. The leaching test showed that the MAG coating protects the adsorbent from CIP leaching. This is ascribed to interactions between the CIP carboxyl groups and magnetite nano-particles. Antibacterial tests showed strong antibacterial activity of the ciprofloxacin-containing adsorbents towards pathogenic *E. coli* and *S. aureus*.

Keywords: natural zeolite; magnetite; ciprofloxacin; adsorption; disinfection

Citation: Kalebić, B.; Pavlović, J.; Dikić, J.; Rečnik, A.; Gyergyek, S.; Škoro, N.; Rajić, N. Use of Natural Clinoptilolite in the Preparation of an Efficient Adsorbent for Ciprofloxacin Removal from Aqueous Media. *Minerals* **2021**, *11*, 518. https://doi.org/10.3390/min11050518

Academic Editor: Francisco Franco

Received: 5 April 2021
Accepted: 5 May 2021
Published: 14 May 2021

1. Introduction

In the last few decades, the use of antibiotics has constantly increased in both human and veterinary medicine. Although some countries have established monitoring systems in order to restrict inappropriate use of antibiotics, water pollution by antibiotics is generally poorly regulated. Different types of antibiotics can be found in both surface waters and in drinking water [1]. Due to their structural complexity, antibiotic molecules are usually very stable, exhibiting a long-lived persistence in the environment and therefore pose a risk to the environment and to human health [2]. They are toxic towards algae and other aquatic organisms and their excessive use leads to bacterial resistance [3,4].

Ciprofloxacin (CIP) is one of the most widely applied fluoroquinolone-type antibiotics for treatment of human and animal bacterial infections because it shows excellent activity against both Gram-positive and Gram-negative bacteria. Its extensive use leads to the presence of fluoroquinolone in waters in a wide range of concentrations. Thus, the CIP concentration in wastewater effluents varies from ng to mg dm^{-3}. An extremely high concentration of up to 50 mg dm^{-3} can be found near drug manufacturing plants [5].

The CIP molecule (Figure 1) has two ionizable groups, amine and carboxyl, with p*Ka* = 5.90 ± 0.15 and 8.89 ± 0.11, respectively. Depending on the pH value, CIP can exist as a cation, zwitterion or anion [6,7].

The removal of CIP from wastewater by conventional wastewater treatments, including oxidation [8], ozonation [9], as well as several photocatalytic [10] and biological treatments [11,12], is usually complex, energy-inefficient, and incomplete [13].

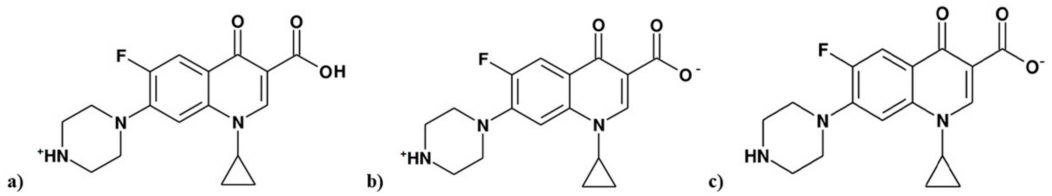

Figure 1. The molecular structures of CIP depending on pH: (**a**) cationic form (in the range 3–6); (**b**) zwitterionic form (in the range 6–9); and (**c**) anionic form (in the range 9–12).

Adsorption is generally regarded as a simple method for the removal of different types of pollutants due to its relatively simple design, easy operation and cost effectiveness. Since the operating cost of a treatment based on the adsorption process is greatly dependent on the cost of the adsorbent material and its recyclability, a variety of low-cost adsorbents have been explored, showing adsorption to be superior in comparison to other methods [14–18]. Thus, carbon-based materials [19–22], clay minerals [23], nano-sized metal oxides [5,24], waste biomaterials [25], biochar [26], coal fly ash [27], as well as different zeolites [28–30] have been studied as adsorbents for the removal of antibiotics from wastewater. Removal efficiency of CIP on different adsorbents are listed in Table 1.

Table 1. Removal efficiency of ciprofloxacin on different types of adsorbent.

Adsorbent	Experimental Conditions	CIP Removal Efficiency, %	Recyclability	Ref.
Nano-sized magnetite	C_0 = 33 mg dm^{-3} Adsorbent dose = 10 g dm^{-3} pH = 5.97 t = 24 h	80	* n.r.	[5]
Graphene hydrogel	C_0 = 50 mg dm^{-3} T = 25 °C $t \approx$ 36 h	75	n.r.	[19]
Carbon from date palm leaflets	C_0 = 100 mg dm^{-3} Adsorbent dose = 2 g dm^{-3} pH = 6 T = 45 °C t = 48 h	56	n.r.	[22]
Halloysite nanotubes	C_0 = 30 mg dm^{-3} Adsorbent dose = 1.7 g dm^{-3} pH = 5–6 T = 20 °C t = 90 min	95	95% after five cycles	[23]
γ-Al_2O_3 nanoparticles	C_0 = 20 mg dm^{-3} Adsorbent dose = 0.775 g dm^{-3} pH = 7.5 t = 46.25 min	53	n.r.	[24]
Biomaterials from banyan aerial roots	C_0 = 60 mg dm^{-3} Adsorbent dose = 1.2 g dm^{-3} pH = 8 T = 25 °C t = 48 h	97	n.r.	[25]
Biochar-montmorillonite	C_0 = 25 mg dm^{-3} Adsorbent dose = 1 g dm^{-3} pH = 5–6 t = 400 min	86	n.r.	[26]

Table 1. *Cont.*

Adsorbent	Experimental Conditions	CIP Removal Efficiency, %	Recyclability	Ref.
Coal fly ash	C_0 = 160 mg dm^{-3} Adsorbent dose = 40 g dm^{-3} T = 40 °C t = 100 min	39	n.r.	[27]
Clinoptilolite	C_0 = 5 mg dm^{-3} Adsorbent dose = 2 g dm^{-3} pH = 6 T = 25 °C	99	n.r.	[29]
Synthesized zeolites (A, X, Y)	C_0 = 150 mg dm^{-3} Adsorbent dose = 0.5 g dm^{-3} pH = 3 T = 20 °C t = 24 h	27–61.4	n.r.	[30]
Commercial zeolites (A, X, Y)	C_0 = 150 mg dm^{-3} Adsorbent dose = 0.5 g dm^{-3} pH = 3 T = 20 °C t = 24 h	34–87	n.r.	[30]

* n.r.—not reported.

It should be noted that the data shown in Table 1 are difficult to compare because they are obtained under different experimental conditions. Moreover, for most adsorbents CIP adsorption is an irreversible process.

Natural zeolites have been extensively studied because of their unique ion-exchange, molecular sieving, and adsorption properties. Their worldwide abundance recommends them as available, low-cost materials [31]. Clinoptilolite (CLI) is the most abundant natural zeolite. Its three-dimensional structure consists of two interconnected micropore channels occupied by exchangeable cations and water molecules. CLI can efficiently remove different pollutants from wastewaters, including inorganic toxic ions such as heavy metal cations [32,33], anions [34,35] as well as various organic species such as pesticides, dyes, or pharmaceuticals [36]. The removal efficacy of CLI can be ascribed to its unique structural features as well as to its propensity to be modified without structural changes. Impregnation of CLI with oxide nanoparticles or with biopolymers leads to an increase of its specific surface and adsorption performance [37–43].

Generally, the literature data on the adsorption of organic pollutants by zeolites are relatively scarce which can be ascribed to the fact that most zeolites are hydrophilic. Hydrophobicity of zeolites increases by the increase of the Si/Al ratio. However, it should be noted that CLI has been the most studied natural zeolite adsorbent not only for inorganic but also for organic pollutants [6]. Its adsorptive effectiveness towards specific pollutants varies because the Si/Al molar ratio and elemental composition of CLI from different regions differ. Among synthetic zeolites, the zeolite Y was reported to be an efficient antibiotic adsorbent [44]. However, the adsorption was found to be irreversible, so the reuse of the spent adsorbent is questionable.

The aim of this research was to study: (1) the adsorptive efficacy of natural clinoptilolite (CLI) for CIP removal at different temperatures and for different initial CIP concentrations, (2) adsorption kinetics and mechanisms, (3) impregnation of CLI with magnetite nanoparticles (MAG-CLI) to allow a facile adsorbent separation, and (4) antibacterial activity of the CIP-containing CLI.

CLI was used for the CIP removal because an extensive study conducted in the last decade showed that clinoptilolite-reach tuffs from Serbia can be perspective adsorbents for the removal of various toxic species [32,33].

2. Materials and Methods

2.1. Materials

The clinoptilolite-rich zeolitic tuff obtained from the Serbian deposit in Slanci (near the capital city of Belgrade) was used as a starting material. Rietveld analysis [45] showed that CLI was the major mineral phase (>80 wt.%), with quartz (<7.5 wt.%) and feldspar (<13 wt.%) the major satellite phases. The cation exchange capacity (CEC), measured by standard procedure [46], was 162.2 mmol M^+/100 g.

Prior to the experiments, the sample was sieved, washed with deionized water to remove impurities, and then dried in an oven at 105 °C overnight to a constant mass. The particle size used in the experiments was in the range of 0.063–0.125 mm since previous studies showed the best adsorptive performance was in particles in that size range [32,33].

All chemicals used were of analytical grade. All the experiments were carried out under controlled conditions. The experiments were performed in a thermostated bath where the temperature was maintained constant to within ±0.1 °C; the CLI samples were weighed to a four-digit accuracy, and the solution concentrations were determined with a four-digit accuracy. In all experiments, deionized water was used.

2.2. Preparation of Magnetite

The magnetite nanoparticles were synthesized per the literature procedure [5,47]. Briefly, $FeCl_3 \cdot 6H_2O$ and $FeCl_2 \cdot 4H_2O$ were dissolved in degassed distilled water under N_2 in a molar ratio of 2:1. A solution of ammonia was then added dropwise to the prepared Fe(II) and Fe(III) solution, increasing the pH to 10. A black solid that precipitated was magnetically separated and washed with distilled water until a negative reaction to chloride ions.

2.3. Preparation of Magnetite-Coated Clinoptilolite (MAG-CLI)

Conversion of CLI to MAG-CLI was carried out following a slightly modified method as described by Mohseni-Bandpi [48]. Briefly, 10 g of CLI were suspended in 120 cm^3 of deionized water and stirred under the N_2 atmosphere at 350 rpm for about 10 min. Then, a solution, which contained $FeCl_3 \cdot 6H_2O$ and $FeSO_4 \cdot 7H_2O$ in a molar ratio of 2:1, was added to the CLI suspension under stirring. The pH of the suspension was adjusted to pH ~10 by the dropwise addition of a water solution of NH_4OH (25 wt.%), followed by a vigorous stirring in a water bath at ~80 °C under N_2 for 1 h. The resulting black precipitate was separated from the suspension by centrifugation and washed several times with deionized water until a negative reaction to chloride ions. Finally, the obtained MAG-CLI was left to dry at 80 °C overnight until constant mass.

2.4. Characterization

2.4.1. Powder X-ray Diffraction Analysis (PXRD)

Analysis of the mineral phases present in the samples was done via the powder X-ray diffraction method (PXRD). PXRD patterns were obtained using a Rigaku SmartLab powder diffractometer (Rigaku, Tokyo, Japan), with CuKα (λ = 1.54178 Å) radiation at 40 kV and 30 mA and Bragg-Brentano focusing geometry. The samples were scanned in the 2θ range from 5° to 65°, with 0.01° step and a scan rate of 5° min^{-1}.

2.4.2. Energy Dispersive X-ray Spectroscopy (EDS)

Elemental compositions of CLI and MAG-CLI were obtained by a Carl Zeiss Supra™ 3VP (Zeiss, Jena, Germany) field-emission gun scanning electron microscope (FEG-SEM) equipped with an EDS detector (Oxford Analysis) with the INCA Energy system for quantification of elements. Before analysis, the samples were coated with gold.

2.4.3. Thermal Analysis

Thermal behavior was examined by simultaneous thermogravimetric (TGA) and differential thermal analysis (DTA) using a SDT Q-600 instrument (TA Instruments, New

Castle, DE, USA). The samples were heated in standard alumina sample cups (90 µL) from room temperature to 800 °C at a heating rate of 10 °C min^{-1} under synthetic air with a flow rate of 100 cm^3 min^{-1}.

2.4.4. Textural Properties

The specific surface area and porosity characteristics were determined by the N_2 adsorption at −196 °C using a Micromeritics ASAP 2020 instrument (Micromeritics, Norcross, GA, USA). Prior to the measurements, the samples were degassed in a vacuum at 423 K for 10 h. The specific surface area of samples was calculated using the Brunauer-Emmett-Teller (BET) method from the linear part of the N_2 adsorption isotherm. The total pore volume (V_{tot}) was determined from the desorption isotherm at p/p_0 = 0.998, and the volume of mesopores was calculated by the Barrett-Joyner-Halenda (BJH) method from the desorption isotherms. The average maximum pore diameter (D_{max}) was determined from the BJH desorption analysis.

2.4.5. TEM Analysis

TEM analysis was carried out at 200 kV using a transmission electron microscope (JEM-2100, JEOL Ltd., Tokyo, Japan) equipped with an ultra-high-resolution objective lens pole piece with a point-to-point resolution of 0.19 nm. The samples were crushed in an agate mortar, dispersed in absolute ethanol, and a fine fraction of the suspension was deposited on Cu holey carbon-coated grids. To determine the average size of magnetite particles, their diameters were measured from the obtained TEM images. Due to the relatively small size of the magnetite nanoparticles, the selected area electron diffraction (SAED) was performed over multiple nanocrystals to obtain the characteristic diffraction rings with the structure-specific *d*-values.

2.4.6. FTIR Analysis

The Fourier transform infrared spectroscopy (FTIR) analysis was performed using a Digilab FTS-80 interferometer (Bio-Rad, Cambridge, MA, USA). The spectra were recorded in the range of 400 to 4000 cm^{-1}, at a resolution of 4 cm^{-1} and 100 scans.

2.4.7. Zeta Potential Measurement

The zeta potentials were measured using a Zetasizer Nano ZS90 (Malvern Instruments Ltd., Malvern, UK) according to the method described by Gulicovski [49]. Briefly, the sample (0.1 g) was suspended in 50 cm^3 of deionized water and left at room temperature overnight. The pH value of the suspension was then adjusted in the range of 2–12 using 0.1 mol dm^{-3} HCl or NaOH. Before measurement, the suspensions were ultrasonically treated for 20 s. The pH values were measured using a Mettler Toledo (Columbus, OH, USA) digital pH meter.

2.4.8. Magnetic Measurements

Magnetic properties were measured using a vibrating sample magnetometer LakeShore 7400 Series VSM (LakeShore, Westerville, OH, USA) at the room temperature and with an applied magnetic field strength of 1.53 T.

2.5. CIP Adsorption Experiments

CIP adsorption experiments were performed at 283, 288 and 293 K by the batch method using 0.2 g of CLI or MAG-CLI in 50 cm^3 of the chosen CIP concentration (15, 25, 50 or 75 mg dm^{-3}). The adsorption experiments were carried out at a pH of 5, which previous studies showed had the best CIP removal efficacy (vide infra). The pH adjusment was performed using HCl or NaOH solutions (0.1 mol dm^{-3}). The suspensions were left shaking (100 rpm) in a thermostated water bath (Memmert, WBE 22) at the chosen temperature for 5 to 60 min. The solid was separated by centrifugation and then filtered through a 0.22 µm nylon filter. The CIP concentration was measured in the filtrate by

standard procedure using a UV-Vis spectrometer, Perkin Elmer Lambda 365 (Perkin Elmer Inc., Waltham, MA, USA) at 278 nm [50]. The amount of the adsorbed CIP per unit of the adsorbent after time t (q_t) was calculated using the following formula:

$$q_e = (C_0 - C_e) \cdot V/m \quad (1)$$

2.6. Leaching Test

Zero point two grams of the spent CLI or MAG-CLI, containing about 21 mg CIP per gram of the adsorbent (CLI or MAG-CLI), were suspended in 50 cm^3 of 0.1 mol dm^{-3} NaCl and left for 24 h in a thermostated water bath at 25 °C. After filtration, the CIP content in the filtrate was determined by UV-Vis. The desorbed amount of CIP was calculated as the ratio of the CIP amount in the solution and on the adsorbent.

The concentration of exchangeable cations (K^+, Mg^{2+} and Ca^{2+}) in filtrates after the CIP adsorption was measured using an atomic absorption spectrophotometer, Varian SpectrAA 55B (SpectraLab Inc., Markham, ON, Canada).

2.7. Antibacterial Activity Test

The antibacterial activity of CIP and of the spent adsorbents (CLI-CIP and MAG-CLI-CIP) was tested towards the Gram-negative bacterium *Escherichia coli* strain DSM 498 and the Gram-positive bacterium *Staphylococcus aureus* strain ATCC 25923. Bacteria were pre-grown on a nutrient agar (NA, Torlak, Serbia) for 16 h at 37 ± 0.1 °C to obtain cultures in the log phase of growth. Prior to the experiments, the samples were sterilized by UV light for 30 min.

The disk diffusion method was used for a qualitative assessment of antibacterial activity. The biomass of each bacterial strain was separately suspended in a sterile physiological solution to achieve the bacterial concentration of about 10^9 CFU cm^{-3} (colony forming units) and then inoculated onto NA with a sterile swab. Antibacterial activity was tested as follows: 0.01 cm^3 of suspensions containing 5, 10 or 20 mg of CIP, CLI-CIP, or MAG-CLI-CIP per cm^3 in a sterile phosphate buffer solution (pH = 7.02) was dropped onto the bacteria inoculated NA and the plates were incubated for 24 h at 37 °C. The results were reported as the presence or absence of the inhibition zone.

3. Results and Discussion

3.1. Powder X-ray Diffraction (PXRD)

The PXRD pattern (Figure 2) showed that CLI was the main mineral phase, displaying diffractions at 2θ = 9.79°, 11.16°, 13.06°, 16.89°, 19.00°, 22.31°, 25.01°, 25.98°, 29.90°, 31.84° and 32.68° [51]. Diffractions at 2θ = 26.6° and 27.1° corresponded to quartz and feldspar, respectively [38,51]. The PXRD pattern of MAG-CLI showed that the modification of CLI to MAG-CLI did not significantly affect the CLI crystallinity. New diffraction peaks that appeared in the pattern of MAG-CLI at 2θ = 35.64°, 43.23° and 62.96° suggest the presence of magnetite Fe_3O_4 [52,53]. According to the EDS analysis (vide infra), the content of magnetite is 12.2 wt.%.

3.2. Energy Dispersive X-ray Spectroscopy (EDS)

The average chemical compositions of CLI and MAG-CLI obtained by the EDS analysis are listed in Table 2. It is evident that the zeolite phase consisted of the calcium-rich clinoptilolite with a Si/Al molar ratio of 5.03. The Si/Al molar ratio increased to 6.12 during modification to MAG-CLI, suggesting a partial dealumination. Moreover, the content of exchangeable cations (Ca and K) decreased in MAG-CLI, whereas the content of Fe increased. Since the content increase of Fe is significantly higher than the content decrease of exchangeable cations, it can be concluded that the modification of CLI to MAG-CLI proceeds not only through an ion exchange but also through precipitation of the Fe species on the CLI surface.

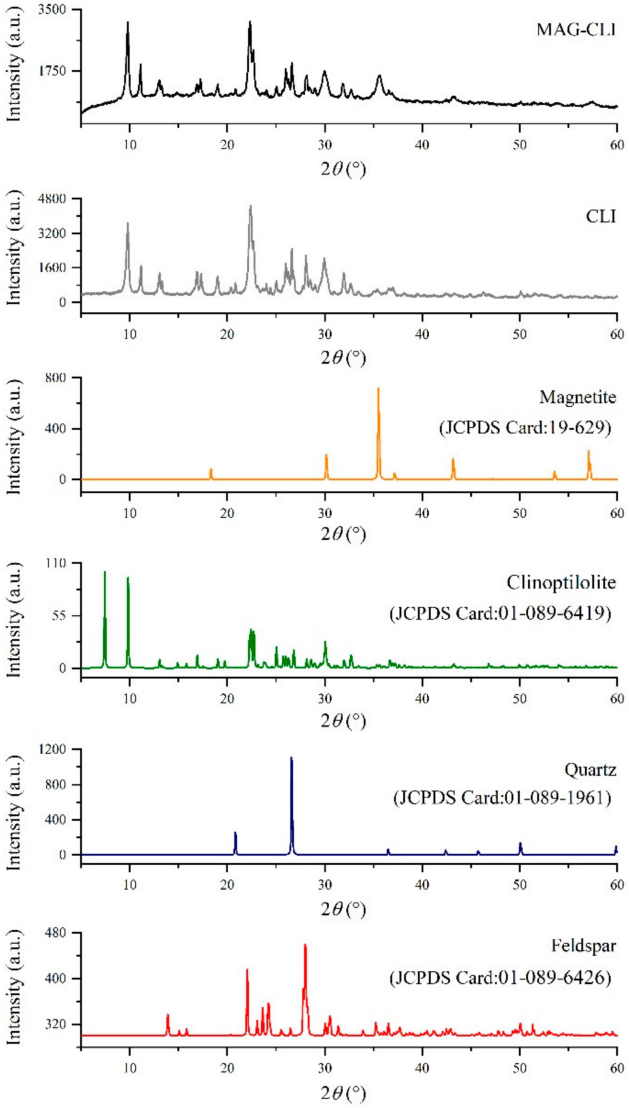

Figure 2. PXRD patterns of CLI and MAG-CLI.

Table 2. The average chemical composition of the CLI phase of CLI and MAG–CLI obtained by EDS analysis.

Sample	Si	Al	O	K	Ca	Fe	Si/Al
				at.%			
CLI	18.35	3.65	75.97	0.44	1.20	0.40	5.03
MAG-CLI	18.39	3.01	72.15	0.27	0.18	5.63	6.12

3.3. Thermogravimetric Analysis (TGA)

The thermograms of CLI and MAG-CLI (Figure 3) show that the TG curves of both samples display similar continual weight loss up to 300 °C. At higher temperatures, the weight loss of MAG-CLI differed from that of CLI. CLI lost weight continuously up to 800 °C, whereas the weight loss of MAG-CLI took place in two stages (300–500 °C and 500–800 °C). The total weight losses were similar (wt.%: 14.2—CLI and 13.1—MAG-CLI). The weight losses are accompanied by the following DTG events: (a) weak DTG maxima at 58, 160 and 600 °C on the DTG curve of CLI, suggesting a release of water molecules from different crystallographic sites in the aluminosilicate lattice, and (b) a strong maximum at 470 °C on the DTG curve of MAG-CLI, indicating a conversion of magnetite to maghemite (γ-Fe_2O_3) [54].

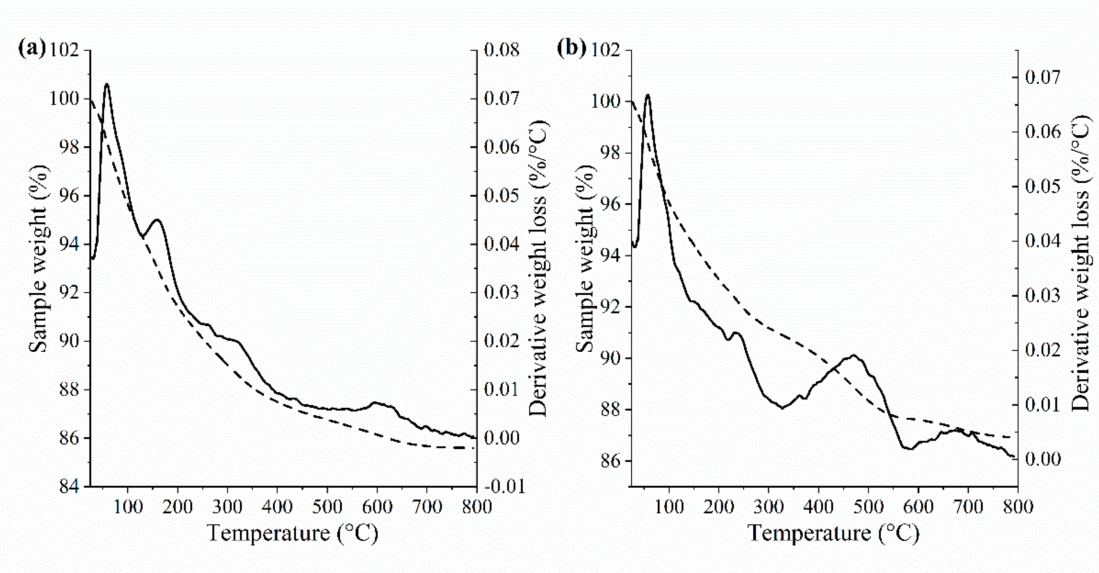

Figure 3. TG (dash) and DTG (solid) curves of CLI (**a**) and MAG-CLI (**b**).

3.4. TEM Analysis

Figure 4 gives the TEM image of MAG–CLI. For comparison, the image of pure magnetite (MAG) is given in Figure 4a. The magnetite particles are in the range of 5–30 nm, with few particles exceeding 100 nm. The selected area electron diffraction (SAED) pattern displays rings typical for the spinel (magnetite) structure, with the most intense ring of the {311} reflections in randomly oriented nanocrystals. MAG shows characteristic octahedral morphology with many crystals connected by the {111} spinel-twin law that forms through self-assembly [55]. On the TEM image of MAG-CLI (Figure 4b) an abundant coverage of the CLI plates by rounded magnetite nanocrystals with highly degraded morphology is evident. The SAED pattern shows interrupted ring patterns that are indicative of nanocrystal ordering. The intensity peaks with a six-fold symmetry, which can be seen for the {111} and {311} magnetite reflections [56,57].

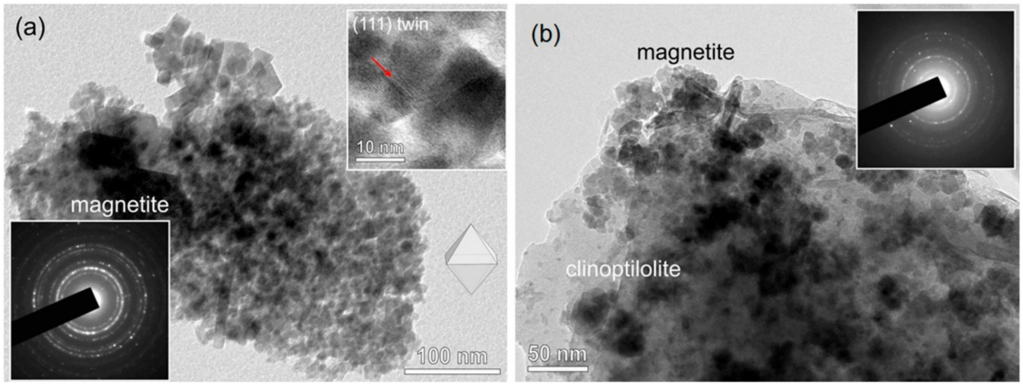

Figure 4. TEM image with SAED pattern of pure MAG (**a**) and MAG-CLI (**b**) samples.

3.5. FTIR Analysis

Figure 5 shows the FTIR spectra of the synthesized samples. The MAG spectrum displays characteristic vibration bands of the Fe–O stretching at about 570 cm^{-1} [47]. The bands overlap with the vibration of the (Al, Si)O_4 tetrahedral units of the aluminosilicate lattice [58]. On the spectra of CLI and MAG-CLI, the stretching vibrations of the OH groups of water molecules (1590–1670 and 3400–3700 cm^{-1}) and of the (Al, Si)O_4 tetrahedral units (1050–1250 cm^{-1}) are evident, confirming that the modification of CLI into MAG-CLI did not influence the zeolite aluminosilicate lattice.

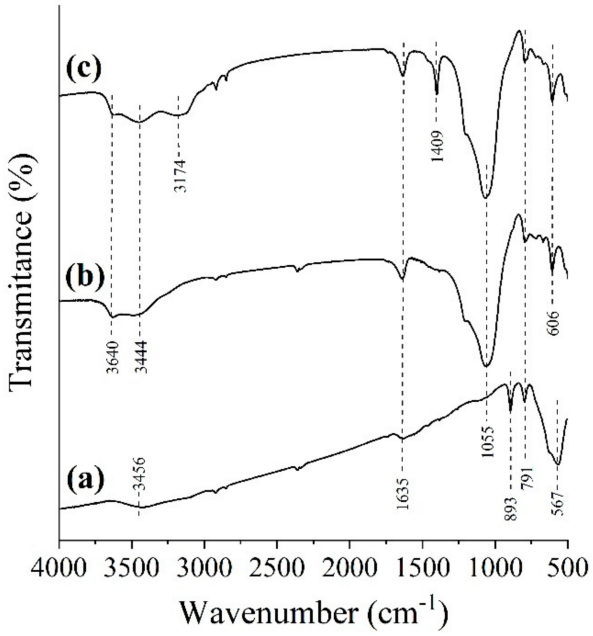

Figure 5. FTIR spectra of MAG (**a**), CLI (**b**) and MAG-CLI (**c**).

3.6. Zeta Potential Measurements

The graphs of the zeta potential as a function of pH (Figure 6) show that the zeta potential of CLI changed by the modification to MAG-CLI, although both CLI and MAG-CLI have a negatively charged surface in a wide pH range from 2 to 12. For MAG-CLI, the point of zero charge (PZC) was at a pH of ~2, which is in accordance with the literature data [59]. The effect of pH on the CIP removal efficiency is presented in Figure 7. The removal efficiency decreased in alkaline media, which is in accord with the fact that both CIP and the surfaces of CLI and MAG-CLI are negatively charged. In acidic media, the CIP is positively charged (CIP^+) and the attractive forces between CIP^+ and CLI/MAG-CLI favor adsorption. The highest removal efficiency is at pH = 5.

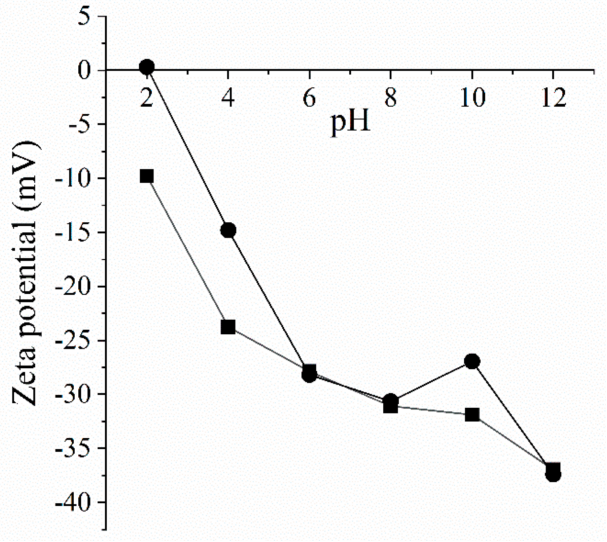

Figure 6. Zeta potential measurements as a function of pH for CLI (square) and MAG-CLI (circle).

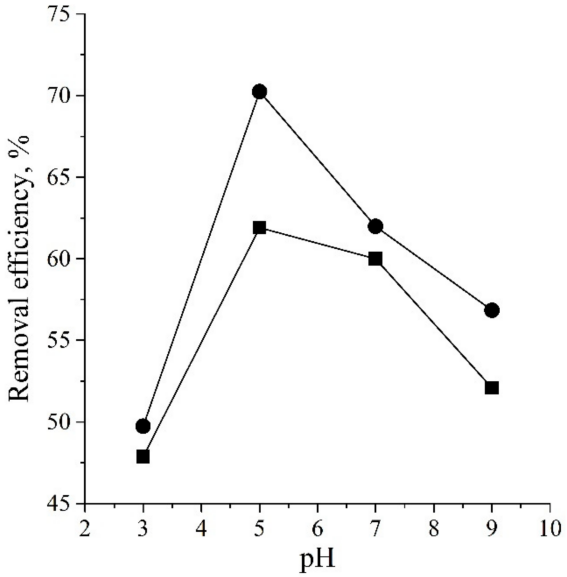

Figure 7. The influence of pH in the CIP adsorption on CLI (squares) and MAG-CLI (circles); C_0 = 50 mg dm^{-3}, adsorption time = 60 min, adsorbent dose = 4 g dm^{-3} and T = 293 K.

Similar results were found for metal oxides, clays, and a graphene oxide composite [5,24,60,61].

3.7. Textural Analysis

Table 3 presents the textural parameters of CLI and MAG-CLI, which show that textural properties changed during conversion. The specific surface area (S_{BET}) of MAG-CLI is two times larger than that of CLI and so is the total pore volume (V_{tot}). The pore size diameter (D_{max}) of MAG-CLI is smaller than in CLI, which could be explained by two phenomena: (1) the formation of a second layer at the CLI surface consisting of magnetite nanoparticles [39,40], and (2) a partial blockage of the CLI pore system caused by the formation of MAG particles.

Table 3. Textural properties of CLI and MAG–CLI.

Sample	S_{BET} (m^2 g^{-1})	V_{tot} (cm^3 g^{-1})	D_{max} (nm)
CLI	23.57	0.0988	16.26
MAG-CLI	45.17	0.1531	3.50

S_{BET}—specific surface area, m^2 g^{-1}; V_{tot}—total pore volume, cm^3 g^{-1}; D_{max}—average maximum pore diameter, nm.

3.8. Magnetic Measurements

The magnetic properties of MAG-CLI were also studied and compared with those of MAG. The magnetization curves are presented in Figure 8a. Both MAG and MAG-CLI showed similar magnetic behavior with the saturation magnetization values of 49.57 and 8.93 emu g^{-1} within magnetic field lower than 1.5 T, respectively. The lower saturation magnetization value of MAG-CLI is the result of MAG precipitation on the CLI surface. However, this value indicates that MAG-CLI possesses magnetic properties since CLI itself does not exhibit magnetism (not shown). Furthermore, the magnetization loops showed an absence of hysteresis, which is a characteristic of the superparamagnetic behavior of some nanoparticles [53]. It is worth noting that MAG-CLI retains magnetic properties after the CIP adsorption (Figure 8b), suggesting that the magnetic separation of the spent MAG-CLI from water media is possible.

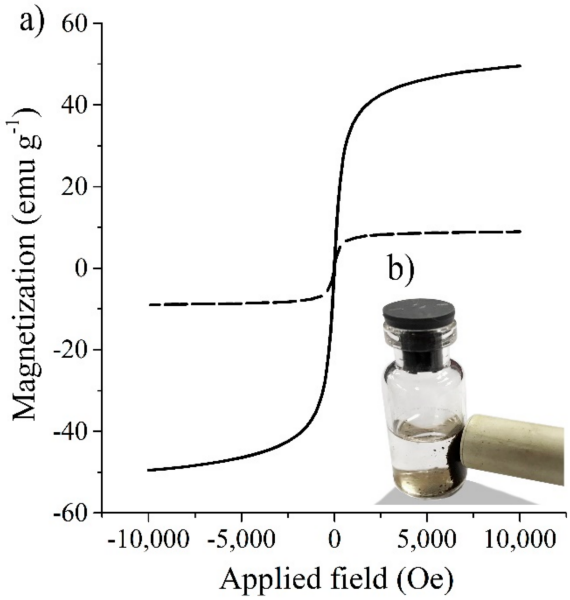

Figure 8. The (**a**) magnetization curve of MAG (solid) and MAG–CLI (dash), and (**b**) magnetic separation of the spent MAG-CLI from suspension.

3.9. Adsorption Isotherm Study

Adsorption of CIP on both CLI and MAG-CLI was studied at 283, 288 and 293 K for the initial CIP concentrations of 15, 25, 50 and 75 mg dm^{-3} and at a pH of 5. The solid to liquid ratio was 1:250, which the experiments had shown to be optimal (Figure 9).

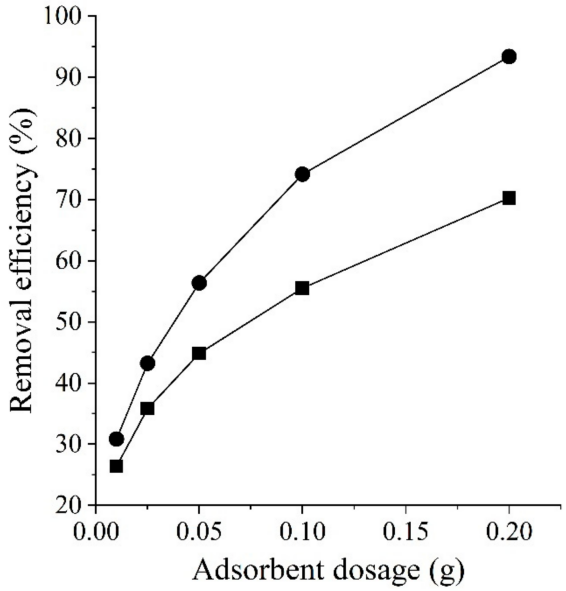

Figure 9. CIP removal as a function of CLI (square) and MAG-CLI (circle) dose (C_0 = 50 mg dm^{-3}, adsorption time = 60 min, T = 298 K and pH = 5).

The adsorption capacity of both CLI and MAG-CLI increased with the initial CIP concentration at all studied temperatures (Figure 10). At 293 K, the adsorption of CIP onto CLI increased from 4.39 mg CIP g^{-1} (for C_0 = 15 mg CIP dm^{-3}) to 12.52 mg CIP g^{-1} (for C_0 = 75 mg CIP dm^{-3}). Similar increases were observed for MAG-CLI: 4.26 mg CIP g^{-1} (for C_0 = 15 mg CIP dm^{-3}) to 12.59 mg CIP g^{-1} (for C_0 = 75 mg CIP dm^{-3}), suggesting that the MAG cover did not influence the CIP adsorption.

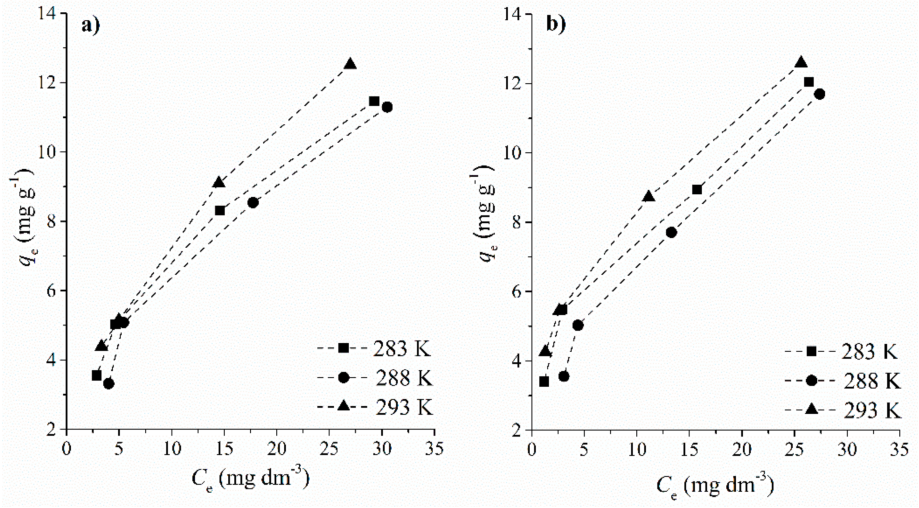

Figure 10. The adsorption isotherms for CIP on CLI (**a**) and MAG-CLI (**b**); q_e is the amount of the adsorbed CIP (mg per 1 g of CLI or MAG-CLI) and C_e is the CIP solution concentration at equilibrium.

The adsorption equilibrium data given in Figure 10 were analyzed by widely applied empirical adsorption isotherm models [17,62]. Among the two-parameter models, only the Langmuir and Freundlich isotherm models gave acceptable fits.

The Langmuir model [63] is represented as:

$$q_e = (q_{max} \cdot b_L \cdot C_e)/(1 + b_L \cdot C_e) \quad (2)$$

where C_e is the equilibrium concentration of CIP (mg dm^{-3}), q_e is the equilibrium concentration of the adsorbed CIP (mg g^{-1}), while q_{max} (mg g^{-1}) and b_L (dm^3 mg^{-1}) are Langmuir constants (q_{max} corresponding to the maximum achievable uptake by the system, and b_L is related to the affinity between CIP and CLI or MAG-CLI).

The Freundlich isotherm model is described with the following equation:

$$q_e = K_f \cdot C_e^{1/n} \quad (3)$$

where C_e is the equilibrium concentration of CIP (mg dm^{-3}), q_e is the equilibrium concentration of the adsorbed CIP (mg g^{-1}), K_f is the Freundlich isotherm constant (mg g^{-1}) and n is a parameter related to the adsorption intensity.

The results are listed in Table 4. As can be seen from the obtained values of the linear regression correlation coefficients (R^2), the Langmuir model gave a slightly better description for the CIP adsorption on both CLI and MAG-CLI. The maximum calculated capacities were 17.30 mg CIP g^{-1} (at 293 K) and 15.86 mg CIP g^{-1} (at 288 K) for CLI and MAG-CLI, respectively. Considering the assumptions of the Langmuir model [63], it could be concluded that one active site at the surface of MAG-CLI is occupied by only one CIP species and that the CIP removal from the water solution proceeds as a monolayer adsorption. Furthermore, the Langmuir separation factor R_L (results not shown) was in the range of 0–1, indicating that the adsorption is a favorable process.

Adsorption Mechanism

The obtained results indicate a strong affinity of both CLI and MAG-CLI towards CIP, which could be explained by electrostatic interactions between the positively charged CIP and negatively charged CLI and MAG-CLI surface. Moreover, the measurements of concentration of exchangeable cations in the filtrate after the CIP adsorption (Table 5) showed that K^+, Mg^{2+}, and Ca^{2+} are present in the filtrate, suggesting that ion exchange reactions occur during adsorption. Since dimensions of the CIP molecule (1.35 × 0.3 × 0.74 nm) [64] exceed the size of the pore openings in the CIP lattice (0.4 nm), the ion exchange likely

takes place only at the surface of the adsorbent. Ion exchange was also proposed as the main adsorption mechanism for the CIP adsorption by montmorillonite [30].

Table 4. The parameters obtained by the adsorption isotherm Equations (2) and (3) for the adsorption of CIP on CLI and MAG-CLI; R^2 is the correlation coefficient.

CLI						
***T*, K**	**Langmuir Isotherm**			**Freudlich Isotherm**		
	q_{max}, mg g^{-1}	b_L, dm^3 mg^{-1}	R^2	K_f, mg g^{-1} (dm^3 mg^{-1})$^{1/n}$	n	R^2
283	14.96	0.1028	0.9944	2.24	2.05	0.9924
288	16.31	0.0697	0.9877	1.73	1.80	0.9804
293	17.30	0.0893	0.9909	2.34	1.97	0.9993
MAG-CLI						
***T*, K**	**Langmuir Isotherm**			**Freundlich Isotherm**		
	q_{max}, mg g^{-1}	b_L, dm^3 mg^{-1}	R^2	K_f, mg g^{-1} (dm^3 mg^{-1})$^{1/n}$	n	R^2
283	13.27	0.2235	0.9834	3.34	2.62	0.9831
288	15.86	0.0914	0.9827	2.16	1.97	0.9809
293	14.25	0.2263	0.9870	3.85	2.81	0.9981

q_{max}—maximum adsorption capacity, mg g^{-1}; b_L—Langmuir constant, dm^3 mg^{-1}; K_f—Freundlich constant, mg g^{-1} (dm^3 mg^{-1})$^{1/n}$; n—adsorption intensity.

Table 5. The concentration of exchangeable cations in filtrates after the CIP adsorption on CLI and MAG-CLI.

Sample	**Cations**		
	K^+	**Mg^{2+}**	**Ca^{2+}**
	mg dm^{-3}		
CLI	0.9325	1.2513	4.2280
MAG-CLI	0.6796	0.3823	2.1890

3.10. Kinetic Analysis

The CIP adsorption dependence on time was investigated at 283, 288 and 293 K for solutions with C_0 = 15, 25, 50 and 75 mg CIP dm^{-3}. Figures 11 and 12 show the CIP uptake from water solution for CLI and MAG-CLI, respectively.

For both CLI and MAG-CLI, the CIP uptake increases rather sharply in the first 10 min, as is evident for all studied temperatures and initial concentrations. Later, the adsorption occurs more slowly. More than 80% of the maximum adsorption capacity was achieved within the first 10 min, indicating fast adsorption kinetics.

The data from Figures 11 and 12 were analyzed using two reaction-based kinetic models and a diffusion-based model. The first model is given by the Lagergren's first-order rate equation [63]:

$$dq_t/dt = k_1\,(q_e - q_t) \quad (4)$$

where q_e (mg g^{-1}) is the adsorption capacity at equilibrium and k_1 (min^{-1}) is the first-order kinetic rate constant. By integrating the Equation (4) using the boundary conditions t = 0 to $t = t$ as well as q_t = 0 (t = 0) and $q_t = q_e$ ($t = t$), the following expression is obtained:

$$\log(q_e - q_t) = \log q_e - (k_1/2.303)\,t \quad (5)$$

The plot of $\log(q_e - q_t)$ vs. t is a straight line if the experimental data follow this kinetic model.

The second reaction–based model that was applied is described by the pseudo-second order rate equation [65]:

$$dq_t/dt = k_2\,(q_e - q_t)^2 \quad (6)$$

Here k_2 (g mg^{-1} min^{-1}) is the rate constant of the pseudo-second order adsorption. Integration between the same limits as above gives the following expression:

$$t/q_t = 1/(k_2\, q_e^2) + (1/q_e)\, t \quad (7)$$

The plot of t/q_t vs. t is a straight line if the experimental data conform to this kinetic model and the values of q_e and k_2 are obtained from the slope and intercept of the plot, respectively.

The influence of diffusion in the CIP adsorption was analyzed by the Weber–Morris mass transfer model [28,58]. The following equation defined this model:

$$q_t = K_{id}\, t^{1/2} + I \quad (8)$$

where K_{id} (mg g^{-1} min$^{-1/2}$) is the intra-particle diffusion rate constant and I (mg g^{-1}) is the parameter related to the thickness of the boundary layer.

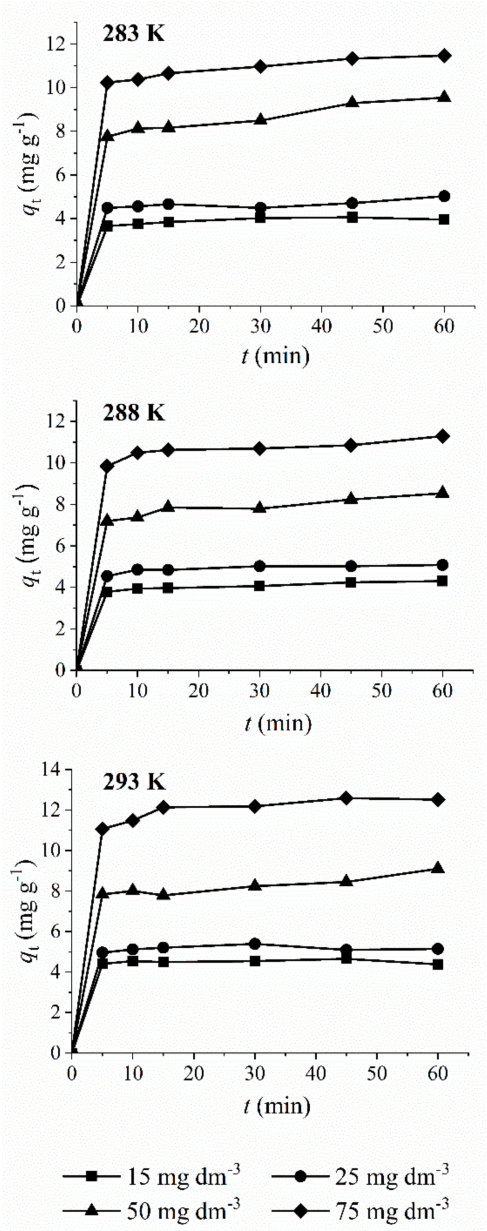

Figure 11. Adsorption kinetics for CIP on CLI for different temperatures; q_t is the amount of the adsorbed CIP (mg per 1 g of CLI) after time t.

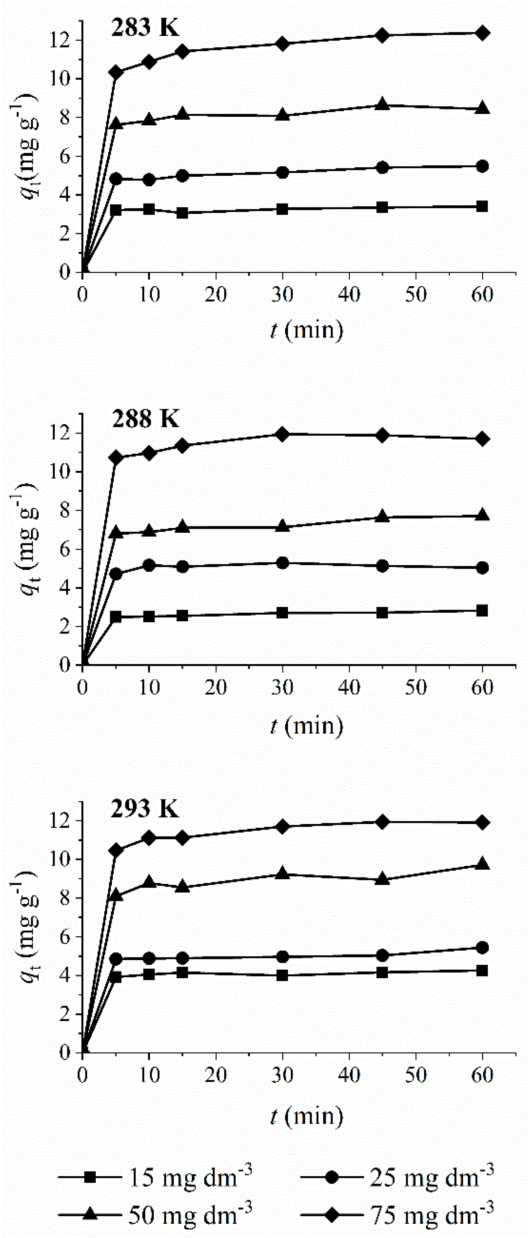

Figure 12. Adsorption kinetics for CIP on MAG-CLI for different temperatures; q_t is the amount of the adsorbed antibiotic (mg per 1 g of MAG-CLI) after time t.

Application of the two reaction-based kinetic models on the experimental data showed that Lagergren's first-order model gives a poor agreement (the results are not shown since the R^2 was lower than 0.80). The pseudo-second order model gives the best fit as judged by the R^2 values (Table 6). This suggests that chemisorption occurs during the CIP adsorption. In addition, the maximum calculated capacities obtained for the highest studied concentration, 13.27 mg CIP g^{-1} (at 293 K) and 13.00 mg CIP g^{-1} (at 283 K) for CLI and MAG-CLI, respectively, correspond to the experimentally obtained values. The Lagergren's pseudo-second order rate constant (k_2) was in the range of 0.0346–0.4011 g mg^{-1} min^{-1} for both CLI and MAG-CLI. The k_2 values changed rather irregularly with temperature for all initial CIP concentrations. A similar phenomenon was reported for the CIP adsorption on clay minerals and on γ-Al_2O_3 [23,24], indicating complexity of the CIP adsorption mechanism.

Table 6. Rate constant for the two studied kinetic models for the adsorption of CIP on CLI and MAG-CLI (R^2 is the correlation coefficient of the linear regression).

CLI							
C_0, mg CIP dm^{-3}	T, K	Weber-Morris Model Parameters			Lagergren's Pseudo-Second-Order Rate Parameters		
		K_{id}, mg g^{-1} min$^{-1/2}$	I, mg g^{-1}	R^2	k_2, g mg^{-1} min^{-1}	q_e, mg g^{-1}	R^2
15	283	0.0729	3.54	0.9301	0.3393	4.09	0.9999
	288	0.0768	3.66	0.9638	0.2490	4.28	0.9998
	293	0.0599	4.29	0.9221	0.2275	4.82	0.9996
25	283	0.0592	4.35	0.7707	0.1896	4.90	0.9988
	288	0.0820	4.50	0.8933	0.2900	5.13	0.9999
	293	0.0377	4.99	0.5450	0.4011	5.24	0.9995
50	283	0.3033	7.15	0.9436	0.0436	9.78	0.9983
	288	0.1946	6.93	0.9386	0.0703	8.63	0.9991
	293	0.1632	7.44	0.8792	0.0714	8.94	0.9989
75	283	0.1442	10.26	0.7653	0.0868	11.58	0.9997
	288	0.1822	9.77	0.7612	0.0886	11.28	0.9991
	293	0.3307	10.46	0.9285	0.0443	13.27	0.9982
MAG-CLI							
C_0, mg CIP dm^{-3}	T, K	Weber-Morris Model Parameters			Lagergren's Pseudo-Second-Order Rate Parameters		
		K_{id}, mg g^{-1} min$^{-1/2}$	I, mg g^{-1}	R^2	k_2, g mg^{-1} min^{-1}	q_e, mg g^{-1}	R^2
15	283	0.0390	3.07	0.7268	0.3133	3.43	0.9997
	288	0.0877	2.24	0.9268	0.1361	3.03	0.9964
	293	0.0434	3.88	0.7702	0.3242	4.26	0.9995
25	283	0.1337	4.46	0.9771	0.1159	5.59	0.9996
	288	0.0399	4.88	0.4335	0.1185	5.08	0.9996
	293	0.0885	4.59	0.8507	0.1257	5.41	0.9980
50	283	0.1972	7.29	0.9393	0.1359	8.60	0.9995
	288	0.1708	6.38	0.9613	0.0861	7.84	0.9993
	293	0.1060	8.21	0.5944	0.0673	8.85	0.9994
75	283	0.3857	9.59	0.7299	0.0346	13.00	0.9930
	288	0.2409	10.12	0.8105	0.0859	12.00	0.9994
	293	0.3047	9.96	0.9832	0.0558	12.46	0.9997

K_{id}—intra-particle diffusion rate constant, mg g^{-1} min$^{-1/2}$; I—parameter related to the thickness of the boundary layer, mg g^{-1}; k_2—pseudo-second-order rate constant, g mg^{-1} min^{-1}; q_e—adsorption capacity, mg g^{-1}.

Table 6 shows that the analysis of the adsorption data by the Weber-Morris mass transfer model gave parameter I values that were higher than one, suggesting that the intra-particle diffusion is not the rate-limiting step [32,65].

3.11. Leaching Test

Leaching of the adsorbed CIP from the spent adsorbents was studied by treating the spent adsorbents in NaCl solution over 24 h. It was found that 20.6% of the CIP is released from CLI (containing 20.2 mg CIP g^{-1}) and 4.40% from MAG-CLI (with 22.1 mg CIP g^{-1}). This suggests the following: (1) magnetite coverage prevents leaching of CIP from the adsorbent, and (2) the CIP adsorption is an irreversible process. The protection of the magnetite coverage could be explained by an interaction of the CIP carboxylic groups with magnetite particles. Namely, adsorptive ability of nano-magnetite was ascribed to the formation of an inner-sphere complex between CIP and magnetite, mediated by carboxylic acid groups [5]. Moreover, the fact that only 20% of the adsorbed CIP can be replaced by Na^+ ions from CLI suggests a strong interaction of CIP and the clinoptilolite surface.

3.12. Regeneration of the Adsorbent

The unsuccessful removal of adsorbed CIP by ion exchange confirms that the adsorption is irreversible. A similar result was also reported for the CIP adsorption onto zeolite A, Y and X [44]. Adsorbent reusability is a very important issue for the operational cost of wastewater treatment based on the adsorption process. With this in mind, we explored a low-temperature atmospheric pressure plasma treatment for the recovery of the spent adsorbent. Plasma treatment is an effective method for the surface modification of various materials including zeolites. Plasma treatments of zeolites were found to increase the removal efficiency of organic species from water after a short treatment time [66,67]. This effect is attributed to an interaction between the reactive species produced in plasma and the zeolite surface [68].

A surface dielectric barrier discharge (SDBD) source with a segmented electrode operating in air was used for plasma treatment of the spent MAG-CLI. Plasma was generated using a 50 Hz sine wave high-voltage signal (V(amplitude) = 12.5 kV) within the d = 2 mm gap between the upper (powered) and lower (grounded) electrode which also served as a sample holder. The duration of the treatment was t = 20 min. The preliminary results of four regeneration cycles are shown in Figure 13.

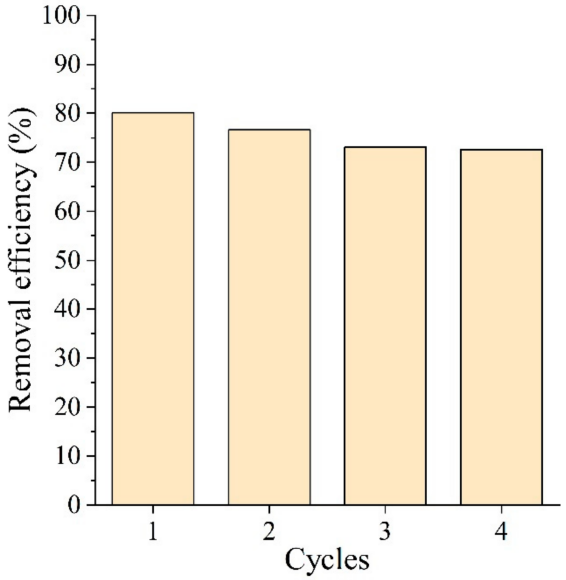

Figure 13. CIP removal efficiency on the MAG-CLI during four adsorption and plasma regeneration cycles (C_0 = 50 mg dm^{-3}, adsorption time = 60 min, T = 298 K and pH = 5).

The results indicate that almost 80% of the adsorbent capacity can be recovered by the plasma treatment (Figure 13). This suggests that such a method is suitable for adsorbent recycling. Further investigation into the optimization of the plasma operational parameters is in progress and will be published.

3.13. Antibacterial Test

In order to make the management of the spent adsorbents cost-effective, antibacterial activity of the CIP-containing CLI and MAG-CLI was tested.

Previously published results showed that clinoptilolite itself does not exhibit antibacterial activity towards tested bacteria strains [69]. Figure 14 shows that CIP has a strong antibacterial effect towards both *E. coli* and *S. aureus*, which is in accordance with the literature data [70,71]. Moreover, according to the inhibition zone, it is evident that both CLI-CIP and MAG-CLI-CIP exhibit a strong antibacterial effect. The effect of the CIP, as well as that of the spent adsorbents, is stronger towards *E. coli* than towards *S. aureus*. This can be explained by differences in structure and composition of the cell wall of Gram-negative and Gram-positive bacteria [72,73]. It is important to note that the CIP concentration used in this assessment was 100 times higher than that on CLI-CIP and MAG-CLI-CIP. This suggests that the CIP immobilized on CLI could be used in water disinfection.

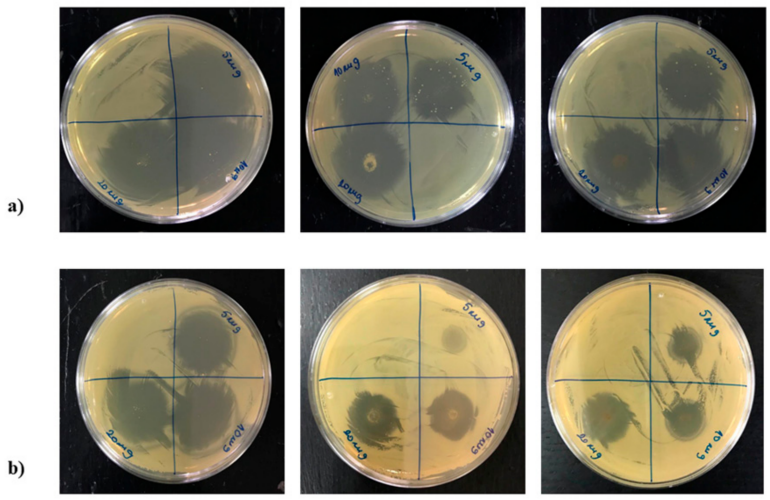

Figure 14. Antibacterial activity of CIP, CLI-CIP and MAG-CLI-CIP towards *E. coli* (**a**) and *S. aureus* (**b**). Initial number of bacteria (t_0): *E. coli* = $1.4 \cdot 10^9$; *S. aureus* = $1.2 \cdot 10^9$ CFU cm^{-3}.

4. Conclusions

From the obtained results, the following can be concluded:

- Calcium-rich natural clinoptilolite shows a high adsorptive activity towards antibiotic ciprofloxacin;
- Clinoptilolite strongly adsorbs ciprofloxacin at a pH of 5 via electrostatic interactions and ion exchange reaction occurring between the ciprofloxacin cations and clinoptilolite;
- The adsorption proceeds quickly following the Lagergren's pseudo-second order rate equation. More than 80% of the maximum adsorption capacity was achieved within the first 10 min for the temperature range of 283 to 293 K;
- Impregnation of clinoptilolite by nano-magnetite particles does not influence the adsorption ability and capacity of clinoptilolite, but brings magnetism to the clinoptilolite-based adsorbent which allows for the easy removal of the spent adsorbent by magnetic separation;
- Magnetite coverage protects the spent adsorbent from the CIP leaching through an interaction of the carboxylic groups of the adsorbed CIP and magnetite particles;
- Preliminary studies indicate that atmospheric pressure plasma could be an efficient method for the regeneration of spent adsorbent;

- Ciprofloxacin-containing clinoptilolite shows strong antibacterial activity towards pathogens (*E. coli* and *S. aureus*), suggesting its possible use in a tertiary stage of water treatment.

Author Contributions: Conceptualization, N.R.; methodology, B.K., J.P. and N.R.; validation, N.R.; formal analysis, B.K., J.P., A.R. and S.G.; investigation, B.K., J.D. and N.Š.; resources, N.R.; data curation, B.K.; writing—original draft preparation, B.K.; writing—review and editing, J.P., J.D., N.Š. and N.R.; visualization, N.R.; supervision, N.R.; project administration, N.R.; funding acquisition, N.R. All authors have read and agreed to the published version of the manuscript.

Funding: This research was funded by the European Union's Horizon 2020 research and innovation program under the Marie Skłodowska-Curie grant agreement, MSCA-ITN-2018, [grant number 812880], and the Ministry of Education, Science and Technological Development of the Republic of Serbia, [grant numbers 451-03-68/2020-14/200287, 451-03-68/2020-14/200135].

Data Availability Statement: All data is shown in the manuscript and raw data is available from corresponding authors upon a request.

Conflicts of Interest: The authors declare no conflict of interest. The funders had no role in the design of the study, in the collection, analyses, or interpretation of data, in the writing of the manuscript, or in the decision to publish the results.

References

1. Kraemer, S.A.; Ramachandran, A.; Perron, G.G. Antibiotic pollution in the environment: From microbial ecology to public policy. *Microorganisms* **2019**, *7*, 180. [CrossRef] [PubMed]
2. Verlicchi, P.; Al Aukidy, M.; Zambello, E. Occurrence of pharmaceutical compounds in urban wastewater: Removal, mass load and environmental risk after a secondary treatment–A review. *Sci. Total Environ.* **2012**, *429*, 123–155. [CrossRef] [PubMed]
3. Frade, V.M.F.; Dias, M.; Teixeira, A.C.S.C.; Palma, M.S.A. Environmental contamination by fluoroquinolones. *Braz. J. Pharm. Sci.* **2014**, *50*, 41–54. [CrossRef]
4. Johnson, A.C.; Keller, V.; Dumont, E.; Sumpter, J.P. Assessing the concentrations and risks of toxicity from the antibiotics ciprofloxacin, sulfamethoxazole, trimethoprim and erythromycin in European rivers. *Sci. Total Environ.* **2015**, *511*, 747–755. [CrossRef]
5. Rakshit, S.; Sarkar, D.; Elzinga, E.J.; Punamiya, P.; Datta, R. Mechanisms of ciprofloxacin removal by nano-sized magnetite. *J. Hazard. Mater.* **2013**, *246–247*, 221–226. [CrossRef]
6. Genç, N.; Dogan, E.C. Adsorption kinetics of the antibiotic ciprofloxacin on bentonite, activated carbon, zeolite, and pumice. *Desalin. Water Treat.* **2013**, *53*, 1–9. [CrossRef]
7. Carabineiro, S.A.C.; Thavorn-Amornsri, T.; Pereira, M.F.R.; Serp, P.; Figueiredo, J.L. Comparison between activated carbon, carbon xerogel and carbon nanotubes for the adsorption of the antibiotic ciprofloxacin. *Catal. Today* **2012**, *186*, 29–34. [CrossRef]
8. Cuerda-Correa, E.M.; Alexandre-Franco, M.F.; Fernández-González, C. Advanced oxidation processes for the removal of antibiotic from water. An overview. *Water* **2020**, *12*, 102. [CrossRef]
9. De Witte, B.; Van Langenhove, H.; Demeestere, K.; Saerens, K.; De Wispelaere, P.; Dewilf, J. Ciprofloxacin ozonation in hospital wastewater treatment plant effluent: Effect of pH and H_2O_2. *Chemosphere* **2010**, *78*, 1142–1147. [CrossRef]
10. Li, W.; Guo, C.; Su, B.; Xu, J. Photodegradation of four fluoroquinolone compounds by titanium dioxide under simulated solar light irradiation. *J. Chem. Technol. Biotechnol.* **2011**, *87*, 643–650. [CrossRef]
11. Li, B.; Zhang, T. Biodegradation and adsorption of antibiotics in the activated sludge process. *Environ. Sci. Technol.* **2010**, *44*, 3468–3473. [CrossRef]
12. Dorival-García, N.; Zafra-Gómez, A.; Navalón, A.; González, J.; Vílchez, J.L. Removal of quinolone antibiotics from wastewater by sorption and biological degradation in laboratory-scale membrane bioreactors. *Sci. Total Environ.* **2013**, *442*, 317–328. [CrossRef]
13. Jia, A.; Wan, Y.; Xiao, Y.; Hu, J. Occurrence and fate of quinolone and fluoroquinolone antibiotics in a municipal sewage treatment plant. *Water Res.* **2012**, *46*, 387–394. [CrossRef]
14. Lin, C.-C.; Lee, C.-Y. Adsorption of ciprofloxacin in water using Fe_3O_4 nanoparticles formed at low temperature and high reactant concentrations in a rotating packed bed with co-precipitation. *Mater. Chem. Phys.* **2020**, *240*, 122049. [CrossRef]
15. Attia, T.M.S.; Hu, X.L.; Qiang, Y.D. Synthesized magnetic nanoparticles coated zeolite for the adsorption of pharmaceutical compounds from aqueous solution using batch and column studies. *Chemosphere* **2013**, *93*, 2076–2085. [CrossRef]
16. Hsini, A.; Essekri, A.; Aarab, N.; Laabd, M.; Addi, A.A.; Lakhmiri, R.; Albourine, A. Elaboration of novel polyaniline@Almond shell biocomposite for effective removal of hexavalent chromium ions and Orange G dye from aqueous solutions. *Environ. Sci. Pollut. Res.* **2020**, *27*, 15245–15258. [CrossRef]

17. Hsini, A.; Naciri, Y.; Benafqir, M.; Ajmal, Z.; Aarab, N.; Laabd, M.; Navío, J.A.; Puga, F.; Boukherroub, R.; Bakiz, B.; et al. Facile synthesis and characterization of a novel 1,2,4,5-benzene tetracarboxylic acid doped polyaniline@zinc phosphate nanocomposite for highly efficient removal of hazardous hexavalent chromium ions from water. *J. Colloid Interface Sci.* **2021**, *585*, 560–573. [CrossRef]
18. Hsini, A.; Naciri, Y.; Laabd, M.; El Ouardi, M.; Ajmal, Z.; Lakhmiri, R.; Boukherroub, R.; Albourine, A. Synthesis and characterization of arginine-doped polyaniline/walnut shell hybrid composite with superior clean-up ability for chromium (VI) from aqueous media: Equilibrium, reusability and process optimization. *J. Mol. Liq.* **2020**, *316*, 113832. [CrossRef]
19. Ma, J.; Yang, M.; Yu, F.; Zheng, J. Water-enhanced removal of ciprofloxacin from water by porous graphene hydrogel. *Sci. Rep.* **2015**, *5*, 13578. [CrossRef]
20. Sun, Y.; Yang, Y.; Yang, M.; Yu, F.; Ma, J. Response surface methodological evaluation and optimization for adsorption removal of ciprofloxacin onto graphene hydrogel. *J. Mol. Liq.* **2019**, *284*, 124–130. [CrossRef]
21. Nogueira, J.; António, M.; Mikhalev, S.M.; Fateixa, S.; Trindade, T.; Daniel-da-Silva, L.A. Porous carrageenan-derived carbon for efficient ciprofloxacin removal from water. *J. Nanomater.* **2018**, *8*, 1004. [CrossRef]
22. El-Shafey, E.-S.I.; Al-Lawati, H.; Al-Sumari, A.S. Ciprofloxacin adsorption from aqueous solution onto chemically prepared carbon from date palm leaflets. *J. Environ. Sci.* **2012**, *24*, 1579–1586. [CrossRef]
23. Cheng, R.; Li, H.; Liu, Z.; Du, C. Halloysite nanotubes as an effective and recyclable adsorbent for removal of low-concentration antibiotics ciprofloxacin. *Minerals* **2018**, *8*, 387. [CrossRef]
24. Najafpoor, A.A.; Sani, O.N.; Alidadi, H.; Yazdani, M.; Fezabady, A.A.N.; Taghavi, M. Optimization of ciprofloxacin adsorption from synthetic wastewater using γ-Al_2O_3 nanoparticles: An experimental design based on response surface methodology. *Colloids Interface Sci. Commun.* **2019**, *33*, 100212. [CrossRef]
25. Fan, H.; Ma, Y.; Wan, J.; Wang, Y.; Li, Z.; Chen, Y. Adsorption properties and mechanisms of novel biomaterials from banyan aerial roots via simple modification for ciprofloxacin removal. *Sci. Total Environ.* **2020**, *708*, 134630. [CrossRef]
26. Ashiq, A.; Sarkar, B.; Adassooriya, N.; Walpita, J.; Rajapaksha, A.U.; Ok, Y.S.; Vithanage, M. Sorption process of municipal solid waste biochar-montmorillonite composite for ciprofloxacin removal in aqueous media. *Chemosphere* **2019**, *236*, 124384. [CrossRef]
27. Zhang, C.-L.; Qiao, G.-L.; Zhao, F.; Wang, Y. Thermodynamic and kinetic parameters of ciprofloxacin adsorption onto modified coal fly ash from aqueous solution. *J. Mol. Liq.* **2011**, *163*, 53–56. [CrossRef]
28. Wang, S.; Peng, Y. Natural zeolites as effective adsorbents in water and wastewater treatment. *Chem. Eng. J.* **2010**, *156*, 11–24. [CrossRef]
29. Ngeno, E.C.; Shikuku, V.O.; Orata, F.; Baraza, L.D.; Kimosop, S.J. Caffeine and ciprofloxacin adsorption from water onto clinoptilolite: Linear isotherms, kinetics, thermodynamic and mechanistic studies. *S. Afr. J. Chem.* **2019**, *72*, 139–142. [CrossRef]
30. Zide, D.; Fatoki, O.; Oputu, O.; Opeolu, B.; Nelana, S.; Olatunji, O. Zeolite 'adsorption' capacities in aqueous acidic media; The role of acid choice and quantification method on ciprofloxacin removal. *Microporous Mesoporous Mater.* **2018**, *255*, 226–241. [CrossRef]
31. Wang, C.-J.; Li, Z.; Jiang, W.-T.; Jean, J.-S.; Liu, C.-C. Cation exchange interaction between antibiotic ciprofloxacin and montmorillonite. *J. Hazard. Mater.* **2010**, *183*, 309–314. [CrossRef]
32. Rajić, N.; Stojaković, D.; Jovanović, M.; Zabukovec Logar, N.; Mazaj, M.; Kaučič, V. Removal of nickle(II) ions from aqueous solutions using the natural clinoptilolite and preparation of nano-NiO on the exhausted clinoptilolite. *Appl. Surf. Sci.* **2010**, *257*, 1524–1532. [CrossRef]
33. Stojaković, D.; Milenković, J.; Daneu, N.; Rajić, N. A study of the removal of copper ions from aqueous solution using clinoptilolite from Serbia. *Clay Clay Miner.* **2012**, *59*, 277–285. [CrossRef]
34. Pavlović, J.B.; Milenković, J.K.; Rajić, N.Z. Modification of natural clinoptilolite for nitrate removal from aqueous media. *J. Serb. Chem. Soc.* **2014**, *79*, 1309–1322. [CrossRef]
35. Jevtić, S.; Arčon, I.; Rečnik, A.; Babić, B.; Mazaj, M.; Pavlović, J.; Matijašević, D.; Nikšić, M.; Rajić, N. The iron(III)-modified natural zeolitic tuff as an adsorbent and carrier for selenium oxyanions. *Microporous Mesoporous Mater.* **2014**, *197*, 92–100. [CrossRef]
36. Muir, B.; Wołowiec, M.; Bajda, T.; Nowak, P.; Czupryński, P. The removal of organic compounds by natural and synthetic surface-functionalized zeolites: A mini-review. *Mineralogia* **2017**, *48*, 145–156. [CrossRef]
37. Ambrozova, P.; Kynicky, J.; Urubek, T.; Nguyen, V.D. Synthesis and modification of clinoptilolite. *Molecules* **2017**, *22*, 1107. [CrossRef]
38. Rajic, N.; Stojakovic, D.; Daneu, N.; Recnik, A. The formation of oxide nanoparticles on the surface of natural clinoptilolite. *J. Phys. Chem. Solids* **2011**, *72*, 800–803. [CrossRef]
39. Ahribesh, A.A.; Lazarević, S.; Janković-Častvan, I.; Jokić, B.; Spasojević, V.; Radetić, T.; Janaćković, Đ.; Petrović, R. Influence of the synthesis parameters on the properties of the sepiolite-based magnetic adsorbents. *Powder Technol.* **2017**, *305*, 260–269. [CrossRef]
40. Javanbakht, V.; Ghoreishi, S.M.; Habibi, N.; Javanbakht, M. A novel magnetic chitosan/clinoptilolite/magnetite nanocomposite for highly efficient removal of Pb(II) ions from aqueous solution. *Powder Technol.* **2016**, *302*, 372–383. [CrossRef]
41. Savić, A.B.; Čokeša, D.; Lazarević, S.; Jokić, B.; Janaćković, D.; Petrović, R.; Živković, L.S. Tailoring of magnetic powder properties for enhanced phosphate removal: Effect of PEG addition in the synthesis process. *Powder Technol.* **2016**, *301*, 511–519. [CrossRef]
42. Arora, M.; Eddy, N.K.; Mumford, K.A.; Baba, Y.; Perera, J.M.; Stevens, G.W. Surface modification of natural zeolite by chitosan and its use for nitrate removal in cold regions. *Cold. Reg. Sci. Technol.* **2010**, *62*, 92–97. [CrossRef]

43. Kragović, M.; Pašalić, S.; Marković, M.; Petrović, M.; Nedeljković, B.; Momčilović, M.; Stojmenović, M. Natural and modified zeolite–alginate composites. Application for removal of heavy metal cations from contaminated water solutions. *Minerals* **2017**, *8*, 11. [CrossRef]
44. Braschi, I.; Blasioli, S.; Gigli, L.; Gessa, C.E.; Alberti, A.; Martucci, A. Removal of sulfonamide antibiotics from water: Evidence of adsorption into an organophilic zeolite Y by its structural modifications. *J. Hazard. Mater.* **2010**, *178*, 218–225. [CrossRef] [PubMed]
45. Coelho, A. *TOPAS Academic 4.1*; Coelho Software: Brisbane, Australia, 2007.
46. Ming, D.W.; Dixon, J.B. Quantitative determination of clinoptilolite in soils by a cation-exchange capacity method. *Clay Clay Miner.* **1987**, *35*, 463–468. [CrossRef]
47. Khalil, M.I. Co-precipitation in aqueous solution synthesis of magnetite nanoparticles using iron(III) salts as precursors. *Arab. J. Chem.* **2015**, *8*, 279–284. [CrossRef]
48. Mohseni-Bandpi, A.; Al-Musawi, T.J.; Ghahramani, E.; Zarrabi, M.; Mohebi, S.; Vahed, S.A. Improvement of zeolite adsorption capacity for cephalexin by coating with magnetic Fe_3O_4 nanoparticles. *J. Mol. Liq.* **2016**, *218*, 615–624. [CrossRef]
49. Gulicovski, J.J.; Čerović, L.S.; Milonjić, S.K. Point of zero charge and isoelectric point of alumina. *Mater. Manuf. Process.* **2008**, *23*, 615–619. [CrossRef]
50. Naveed, S.; Waheed, N. Simple UV spectrophotometric assay of ciprofloxacin. *MJPMS* **2014**, *3*, 10–13.
51. Hawash, H.B.I.; Chmielewska, E.; Netriová, Z.; Majzlan, J.; Pálková, H.; Sokolík, R. Innovative comparable study for application of iron oxyhydroxide and manganese dioxide modified clinoptilolite in removal of Zn(II) from aqueous medium. *J. Environ. Chem. Eng.* **2018**, *6*, 6489–6503. [CrossRef]
52. Rajput, S.; Pittman, C.U., Jr.; Mohan, D. Magnetic magnetite (Fe_3O_4) nanoparticles synthesis and applications for lead (Pb^{2+}) and chromium (Cr^{6+}) removal from water. *J. Colloid Interface Sci.* **2016**, *468*, 334–346. [CrossRef] [PubMed]
53. Kouli, M.-E.; Banis, G.; Tsarabaris, P.; Ferraro, A.; Hristoforou, E. A study on magnetic removal of sodium, calcium and potassium ions from seawater using magnetite/clinoptilolite–Na composite nanoparticles. *J. Magn. Magn. Mater.* **2018**, *465*, 692–699. [CrossRef]
54. Attia, T.M.S.; Hu, X.L.; Yin, D.Q. Synthesised magnetic nanoparticles coated zeolite (MNCZ) for the removal of arsenic (As) from aqueous solution. *J. Exp. Nanosci.* **2014**, *9*, 551–560. [CrossRef]
55. Rečnik, A.; Nyirő-Kósa, I.; Dódony, I.; Pósfai, M. Growth defects and epitaxy in Fe_3O_4 and γ-Fe_2O_3 nanocrystals. *Cryst. Eng. Comm.* **2013**, *15*, 7539–7547. [CrossRef]
56. Nyirő-Kósa, I.; Rečnik, A.; Pósfai, M. Novel methods for the synthesis of magnetite nanoparticles with special morphologies and textured assemblages. *J. Nanopart. Res.* **2012**, *14*, 1150–1159. [CrossRef]
57. Jordan, V.; Javornik, U.; Plavec, J.; Podgornik, A.; Rečnik, A. Self-assembly of multilevel branched rutile-type TiO_2 structures via oriented lateral and twin attachment. *Sci. Rep.* **2016**, *6*, 24216. [CrossRef]
58. Lin, H.; Liu, Q.-L.; Dong, Y.-B.; He, Y.-H.; Wang, L. Physicochemical properties and mechanism study of clinoptilolite modified by NaOH. *Microporous Mesoporous Mater.* **2015**, *218*, 174–179. [CrossRef]
59. Cotton, A. Dissolution kinetics of clinoptilolite and heulandite in alkaline conditions. *Biosci. Horiz.* **2008**, *1*, 38–43. [CrossRef]
60. Duan, W.; Wang, N.; Xiao, W.; Zhao, Y.; Zheng, Y. Ciprofloxacin adsorption onto different micro-structured tourmaline, halloysite and biotite. *J. Mol. Liq.* **2018**, *269*, 874–881. [CrossRef]
61. Wang, F.; Yang, B.; Wang, H.; Song, Q.; Tan, F.; Cao, Y. Removal of ciprofloxacin from aqueous solution by a magnetic chitosan grafted graphene oxide composite. *J. Mol. Liq.* **2016**, *222*, 188–194. [CrossRef]
62. Ullah, S.; Azmi, B.M.; Ali, A.M.; Al-Sehemi, A.G.; Gonfa, G.; Mukhtar, A.; Abdul Kareem, F.A.; Ayoub, M.; Saqib, S.; Binti Mellon, N. Synthesis and characterization of mesoporous MOF UMCM-1 for CO_2/CH_4 adsorption; an experimental, isotherm modeling and thermodynamic study. *Microporous Mesoporous Mat.* **2020**, *294*, 1387–1811. [CrossRef]
63. Langmuir, I. The adsorption of gases on plane surfaces of glass, mica, and platinum. *J. Am. Chem. Soc.* **1918**, *40*, 1361–1403. [CrossRef]
64. Ma, S.; Si, Y.; Wang, F.; Su, L.; Xia, C.; Yao, J.; Chen, H.; Liu, X. Interaction processes of ciprofloxacin with graphene oxide and reduce graphene oxide in the presence of montmorillonite in simulated gastrointestinal fluids. *Sci. Rep.* **2017**, *7*, 2588.
65. Weber, W.J., Jr.; Morris, J.C. Advances in Water Pollution Research: Removal of biologically resistant pollutants from waste waters by adsorption. In *Proceedings of the International Conference on Water Pollution Symposium*; Pergamon Press: London, UK, 1962.
66. Mirzaei, H.; Almasian, M.R.; Mousavian, S.M.A.; Kalal, H.S. Plasma modification of a natural zeolite to improve its adsorption capacity of strontium ions from water samples. *Int. J. Environ. Sci. Technol.* **2019**, *16*, 6157–6166. [CrossRef]
67. Garcia, J.J.M.; Nuñez, J.A.P.; Salapare, H.S.; Vasquez, M.R., Jr. Adsorption of diclofenac sodium in aqueous solution using plasma-activated natural zeolites. *Results Phys.* **2019**, *15*, 102629. [CrossRef]
68. Kogelschatz, U. Dielectric-barrier discharges: Their history, discharge physics, and industrial applications. *Plasma Chem. Plasma Proc.* **2003**, *23*, 1–46. [CrossRef]
69. Hrenovic, J.; Milenkovic, J.; Ivankovic, T.; Rajic, N. Antibacterial activity of heavy metal-loaded natural zeolite. *J. Hazard. Mater.* **2012**, *201–202*, 260–264. [CrossRef]
70. Simões, M.; Rocha, S.; Coimbra, M.; Vieira, M. Enhancement of *Escherichia coli* and *Staphylococcus aureus* antibiotic susceptibility using sesquiterpenoids. *J. Med. Chem.* **2008**, *4*, 616–623. [CrossRef]

71. Chalkley, L.J.; Koornhof, H.J. Antimicrobial activity of ciprofloxacin against *Pseudomonas aeruginosa*, *Escherichia coli*, and *Staphylococcus aureus* determined by the killing curve method: Antibiotic comparisons and synergistic interactions. *Antimicrob. Agents Chemother.* **1985**, *28*, 331–342. [CrossRef]
72. Berlanga, M.; Montero, M.T.; Hernández-Borrell, J.; Viñas, M. Influence of the cell wall on ciprofloxacin susceptibility in selected wild-type Gram-negative and Gram-positive bacteria. *Int. J. Antimicrob. Agents* **2004**, *23*, 627–630. [CrossRef]
73. Mohsen, E.; El-Borady, O.M.; Mohamed, M.B.; Fahim, I.S. Synthesis and characterization of ciprofloxacin loaded silver nanoparticles and investigation of their antibacterial effect. *J. Radiat. Res. Appl.* **2020**, *13*, 416–425. [CrossRef]